magnetochemistry

MDPI

Article

Relationship between the Coordination Geometry and Spin Dynamics of Dysprosium(III) Heteroleptic Triple-Decker Complexes

Tetsu Sato [1], Satoshi Matsuzawa [2], Keiichi Katoh [1,*], Brian K. Breedlove [1] and Masahiro Yamashita [1,3,4,*]

[1] Department of Chemistry, Graduate School of Science, Tohoku University, Aramaki-Aza-Aoba, Aoba-ku, Sendai 980-8578, Japan; tetsu.sato.r1@dc.tohoku.ac.jp (T.S.); breedlove@m.tohoku.ac.jp (B.K.B.)
[2] Institute for Materials Research, Tohoku University, 2–1-1 Katahira, Aoba-ku, Sendai 980-8577, Japan; matsuzawa@imr.tohoku.ac.jp
[3] Advanced Institute for Materials Research, Tohoku University, 2–1-1 Katahira, Aoba-ku, Sendai 980-8577, Japan
[4] School of Materials Science and Engineering, Nankai University, Tianjin 300350, China
* Correspondence: keiichi.katoh.b3@tohoku.ac.jp (K.K.); yamasita@agnus.chem.tohoku.ac.jp (M.Y.); Tel.: +81-22-795-6547 (K.K.); +81-22-795-6544 (M.Y.)

Received: 10 August 2019; Accepted: 22 November 2019; Published: 26 November 2019

Abstract: When using single molecule magnets (SMMs) in spintronics devices, controlling the quantum tunneling of the magnetization (QTM) and spin-lattice interactions is important. To improve the functionality of SMMs, researchers have explored the effects of changing the coordination geometry of SMMs and the magnetic interactions between them. Here, we report on the effects of the octa-coordination geometry on the magnetic relaxation processes of dinuclear dysprosium(III) complexes in the low-temperature region. Mixed ligand dinuclear Dy^{3+} triple-decker complexes [(TPP)Dy(Pc)Dy(TPP)] (**1**), which have crystallographically equivalent Dy^{3+} ions, and [(Pc)Dy(Pc)Dy(TPP)] (**2**), which have non-equivalent Dy^{3+} ions, (Pc^{2-} = phthalocyaninato; TPP^{2-} = tetraphenylporphyrinato), undergo dual magnetic relaxation processes. This is due to the differences in the ground states due to the twist angle (φ) between the ligands. The relationship between the off-diagonal terms and the dual magnetic relaxation processes that appears due to a deviation from D_{4h} symmetry is discussed.

Keywords: Dy^{3+} ion; triple-decker; spin dynamics; octa-coordination geometry

1. Introduction

Rational design and synthesis of single molecular magnets (SMMs) and molecular nanomagnets (MNMs) suitable for quantum information processing (QIP) in quantum computers (QCs) remains difficult [1–7]. Over the past two decades, a wide range of SMMs with controlled spin relaxation processes and high performance have been reported. The charge density distribution of oblate-type lanthanoid ions, (like terbium(III) and dysprosium(III)), strongly improves axial coordination properties of square antiprism (D_{4d}), pentagonal bipyramidal (D_{5h}), and "vent metallocene" type complexes (SMM characteristics have been confirmed for C_1 symmetry) [8–10]. In the D_{4d} ligand field system, the SMM characteristics can be controlled by manipulating the ground state via rotation of the ligands by protonation/deprotonation [11,12], coupling of Tb^{3+}-bisphthalocyaninato (Pc^{2-}) complex with cadmium ions, etc. [13]. Recently, several groups have shown the relationship between octa-coordination environments and the magnetic relaxation processes of Tb^{3+}-Pc^{2-} multiple-decker SMMs along the C_4 rotation axis. From these reports, correlations between the twist angle (φ), ligand field (LF) parameters, and the lowest ground state of Pc^{2-} have been clarified [14]. However, the influence of the coordination environment on the spin relaxation phenomena is not completely understood. In the case of Dy^{3+} ions, the magnetic relaxation mechanism strongly depends on the electronic structure and can sometimes be complicated. In 2003, Ishikawa and coworkers determined that the lowest ground states (J_z) of the $DyPc_2$ complex to be $|J_z| = 13/2$ by using magnetic measurements when φ is 45° and $|J_z| = 11/2$ when φ is 32° [15,16]. In our previous work, we have shown that for some complexes with two crystallographically equivalent Dy^{3+} ions, the ground state is split by the Zeeman effect only if the angle is 45°, resulting in dual relaxation processes. There have been other attempts to elucidate the identities of the dual processes by using theoretical and experimental approaches. Thus, it is important to carefully design the coordination environment around the Dy^{3+} ion in order to investigate the correlation between the magnetic relaxation process and the ground state in detail. In other words, due to the sensitivity toward the coordination environment, Dy^{3+} complexes are easier to control than Tb^{3+} complexes. In this paper, in addition to the dinuclear Dy^{3+} triple-decker complexes we have reported so far, we discuss the relationship between coordination environment and magnetic properties for (TPP)Dy(Pc)Dy(TPP)] (**1**) and [(Pc)Dy(Pc)Dy(TPP)] (**2**) (Pc^{2-} = phthalocyaninato and TPP^{2-} = tetraphenylporphyrinato) with C_4 symmetry.

2. Results and Discussion

2.1. Synthesis and Crystal Strucures

We synthesized the compounds following reported procedures [17]. Single crystal X-ray diffraction analyses on triple-decker complexes **1** and **2** were performed to investigate the coordination environment around the Dy^{3+} ions (Table S1). For **1**, which crystallized in the tetragonal space group $I4/m$, the twist angle (φ) between the outer TPP^{2-} ligand and the inner Pc ligand was determined to be 4°. Therefore, the coordination environment around the Dy^{3+} ions has a slightly distorted square-prism (SP) structure. Since the inner Pc^{2-} ligand acts as a mirror plane in the molecule, the two Dy^{3+} ions are equivalent, and the distance between them was determined to be 3.71 Å. This is a relatively long value among the dinuclear Dy^{3+} triple-decker complexes reported so far. Compound **2** crystallized in the monoclinic space group $C2_1/c$, and the Dy^{3+} ions are inequivalent. φ between the outer and the inner Pc^{2-} ligands was determined to be 39°, meaning that it has a square-antiprism (SAP) structure. φ between the inner Pc^{2-} ligand and the TPP^{2-} ligand was 14°, which is indicative of a highly distorted SAP structure.

Besides the φ between the ligands in the multi-decker type SMM [18], the distance between the coordination isoindole nitrogen atom (N_{iso}) and the metal ions (d), and the angles between the C_4 axis and the direction of Dy^{3+}–N_{iso} (α) affect the properties of these type of SMMs [19]. From a comparison of **1** and **2** with previously studied Dy^{3+} triple-decker complexes **1**–**6** (Table 1) [20,21], site A of **1** and **2** involving a TPP^{2-} ligand has a small φ. Moreover, distances d_2 and d_3 between the N_{iso} of the Pc^{2-} ligand and the metal ions, as indicated in Figure 1, are greater than those in other complexes. **6** has a large d_2 at the small φ site, and φ decreases with increases in d_2 and d_3. In other words, the TPP^{2-} ligands strongly push the Dy^{3+} ions to the outside of the complex.

The ground states of the Dy^{3+} ions can be estimated from the structure, and theoretical calculations of electrostatic potentials distributed over α for the 4f-shells indicate that the ground state $|J_Z|$ is highly dependent on $\alpha$and d [22]. The ground states of **1** and **2** were estimated from the data in Table 1, and $|J_Z| =$ 11/2 and 13/2 are the lowest ground states, respectively. However, the $|J_Z|$ levels of these dinuclear Dy^{3+} triple-decker complexes are known to mix [19], and intermediate $|J_Z|$ levels have the lowest basal order since α is near the magic angle of 54.7° [20,21]. Therefore, φdetermines the ground states of the Dy^{3+} ions.

Crystal packing diagrams for **1** and **2** are shown in Figure 2. The intermolecular Dy^{3+}-Dy^{3+} distances along the c axis in **1** and **2** were determined to be 13.61 Å and 11.63 Å, respectively. The molecules of **1** and **2** are rather well-separated from neighboring molecules due to the tetraphenyl groups of the TPP^{2-} ligands and chloroform molecules as crystal solvents (Table S2). Furthermore, PXRD patterns for **1** and **2** at 293 K are slightly different from those simulated from X-ray single crystallographic data for **1** at 120 K because of partial elimination of crystal solvents (Figure S7). From elemental analysis, some of the crystal solvent desorbed. However, the magnetic properties of the same sample remained unchanged after several months, meaning that solvent desorption has little effect on the magnetic properties. The crystal system is the same regardless of whether a solvent is present or absent, meaning that it does not affect the magnetic measurements.

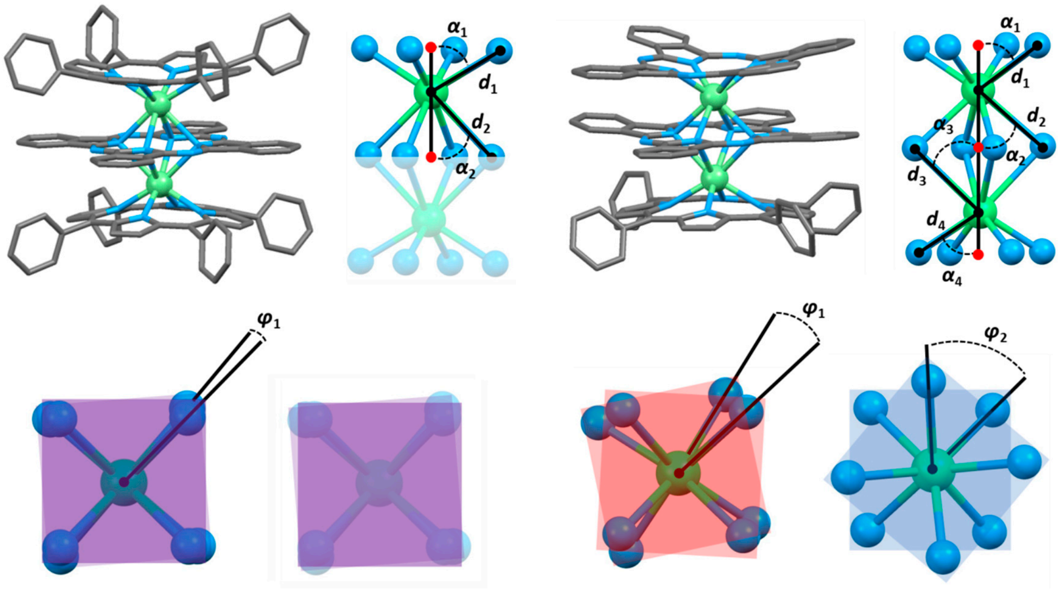

(**a**) (**b**)

Figure 1. Top and side views of (**a**) [(TPP)Dy(Pc)Dy(TPP)] (**1**) and (**b**) [(Pc)Dy(Pc)Dy(TPP)] (**2**). The bottom of (**a**) and (**b**) are enlargements of the coordination spheres around the Dy^{3+} ions. H atoms and crystal solvents are omitted for clarity. Dy^{3+}: light green, C: grey, and N: light blue.

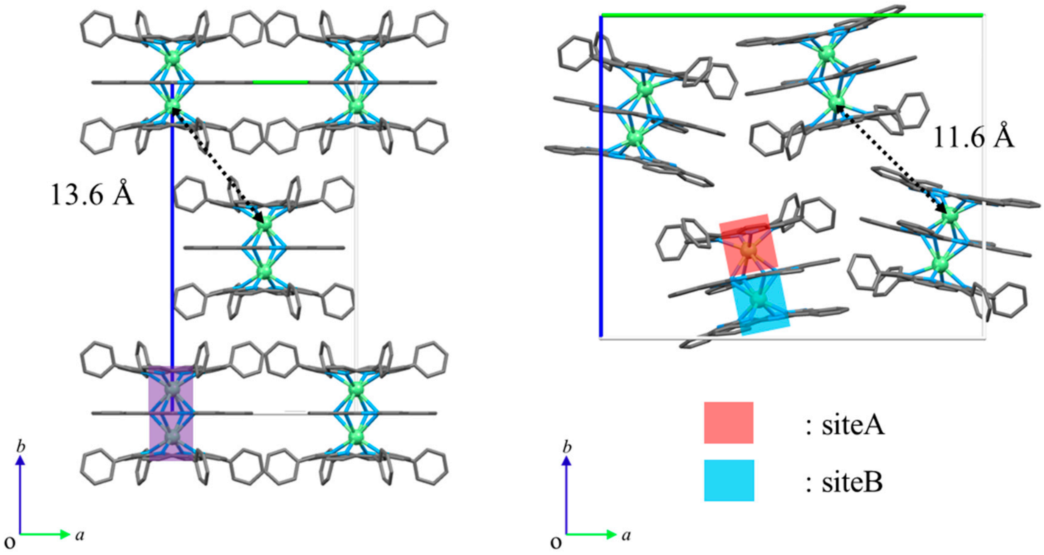

(**a**) (**b**)

Figure 2. Packing diagrams for (**a**) [(TPP)Dy(Pc)Dy(TPP)] (**1**) and (**b**) [(Pc)Dy(Pc)Dy(TPP)] (**2**). Intermolecular Dy^{3+} distances indicated by black dotted arrows. H atoms and crystal solvents are omitted for clarity. Dy^{3+}: light green, C: grey, and N: light blue.

Table 1. Selected crystallographic data for Dy^{3+}-Pc triple-decker complexes.

Complex	α_1 [°]	α_2 [°]	α_3 [°]	α_4 [°]	d_1 [Å]	d_2 [Å]	d_3 [Å]	d_4 [Å]	φ_A [°]	φ_B [°]
[(TPP)Dy(Pc)Dy(TPP)] **1**	59	46	46	59	2.39	2.67	2.67	2.39	4	4
[(Pc)Dy(Pc)Dy(TPP)] **2**	57	49	45	60	2.35	2.57	2.72	2.37	39	14
[(Pc)Dy(ooPc)Dy(Pc)] **3** [a]	57	48	48	57	2.35	2.59	2.59	2.35	45	45
[(ohPc)Dy(ohPc)Dy(ohPc)] **4** [b]	57	47	47	57	2.35	2.60	2.60	2.35	27	27
[(obPc)Dy(obPc)Dy(obPc)] **5** [c]	57	48	48	57	2.35	2.60	2.60	2.35	32	32
$[Dy_4]$ **6** [d]	57	46	49	57	2.33	2.65	2.53	2.37	23	45

[a] ooPc = 2,3,9,10,16,17,23,24-octakis(octyloxy)phthalocyaninato; [b] $ohPc^{2-}$ = 2,3,9,10,16,17,23,24-octakis(hexyloxy) phthalocyaninato; [c] $obPc^{2-}$ = 2,3,9,10,16,17,23,24-octakis(butoxy)phthalocyaninato; [d] $[Dy(obPc)_2]$Dy(Fused-Pc) $Dy[Dy(obPc)_2]$ (Fused-Pc^{4-} = bis{72,82,122,132,172,182-hexabutoxytribenzo[g, l, q]-5, 10, 15, 20-tetraazaporphirino}[b, e]benzenato).

2.2. Static Magnetic Properties

The static magnetic susceptibility of **1** and **2** were measured in the T range of 1.8–300 K using a superconducting quantum interference device (SQUID) magnetometer. The $\chi_M T$ value at 300 K is consistent with the value expected for the two Dy^{3+} ions ($^6H_{15/2}$, S = 5/2, L = 5, g = 4/3). Curie–Weiss plots for **1** and **2** are shown in Figure 3. Linear approximation was performed over the entire T range to obtain values of the Curie (C) (28.50 cm^3 K mol^{-1} (**1**) and 28.20 cm^3 K mol^{-1} (**2**)) and Weiss constants (θ) (–2.33 K (**1**) and –1.97 K (**2**)) (Figures S8 and S9). In $\chi_M T$ versus T plots, the values for **1** decreased with a decrease in T, reaching a minimum of 19.9 cm^3 K mol^{-1} at 1.8 K, which indicates that magnetic properties of the Dy^{3+} complexes mainly originate from LF effects, such as thermal depopulation of the Stark sublevels [23–25]. As for **2**, there was a slight increase in the $\chi_M T$ values when T < 4 K. Since the intermolecular metal distance is sufficiently long [26], the increase is thought to be due to the magnetic dipole interactions between the Dy^{3+} ions in the molecule. All Dy^{3+}-Pc complexes so far reported exhibit similar ferromagnetic behavior. However, the behavior of the $\chi_M T$ values for **1** is different from the other Dy^{3+} triple-decker complexes, and an increase in the $\chi_M T$ values was not observed in the low T region. Although the fact that the intermolecular distance is similar for each complex, the difference in LF parameters of the Dy^{3+} ions has a dramatic effect. In other words, the increase in the off-diagonal terms and the change in the LF splitting energy along with the change in symmetry are important factors affecting the magnetic behavior. Fitting of the data was performed using the PHI program with reported LF parameters [27]. However, we could not obtain consistent results for **1** and **2** because their ground states are complicated due to mixing of the off-diagonal terms.

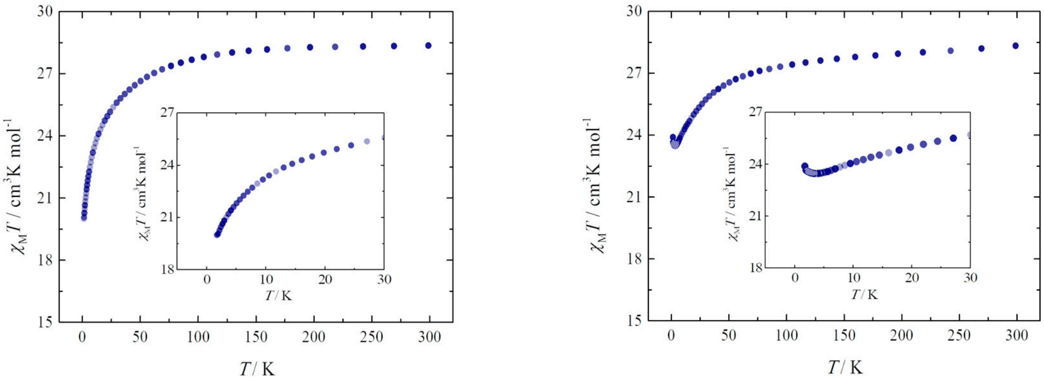

(**a**) (**b**)

Figure 3. T dependence of $\chi_M T$ measured on powder samples of (**a**) **1** and (**b**) **2** in the T range of 1.8–300 K in an H_{dc} of 0.5 kOe. The inset is a magnified plot of 1.8–30 K.

In order to confirm the magnetic anisotropy of the molecule, T dependence of MH were performed (Figure 4). For both complexes, the magnetization did not saturate up to 70 kOe. However, splitting of the M versus HT^{-1} plot occurred, indicating that not only depopulation occurred but also both complexes had large magnetic anisotropies. In addition, butterfly-type hysteresis was not observed during the MH measurements at 1.8 K. When uniaxial anisotropy is strong, the saturation magnetization value (M_s) is expressed as $M_s = 1/2 \times g^*(z) \times \widetilde{S}$ where $\widetilde{S} = 1/2$ [28]. So, the M_s values of **1** and **2** were $M_s = 8.6\ \mu_B$ and $M_s = 7.4\ \mu_B$, calculated using $|J_z| = 13/2$ ($g^*(x) = g^*(y) = 0$, $g^*(z) = 17.3$) and 11/2 ($g^*(x) = g^*(y) = 0$, $g^*(z) = 14.7$), respectively. Although the measured values are larger than the calculated values (**1**: 13.6 μ_B, **2**: 13.7 μ_B), they are smaller than the effective magnetic moments (μ_{eff}) of two Dy^{3+} ions ($\mu_{eff} = 21\ \mu_B$).

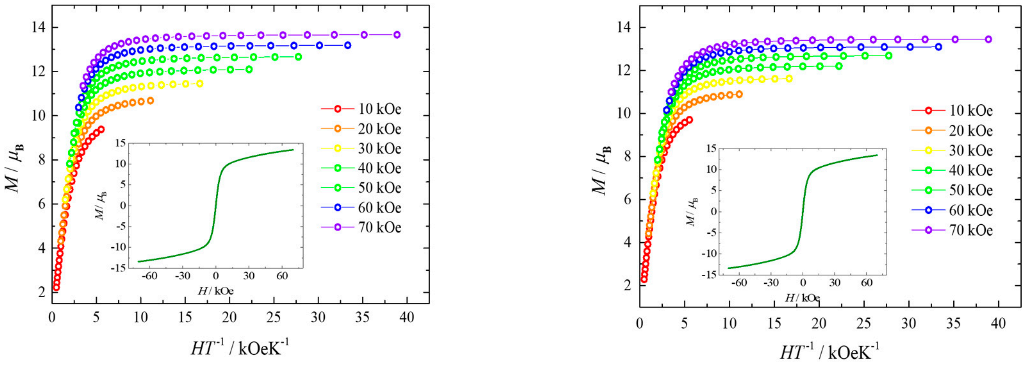

(**a**) (**b**)

Figure 4. Magnetic field (H) dependence of the magnetization (M) for powder samples of (**a**) **1** and (**b**) **2** in the T range of 1.8–20 K.

2.3. Dynamic Magnetic Properties

In order to investigate the magnetic relaxation processes, alternating current (ac) magnetic susceptibility measurements were performed on powder samples of **1** and **2**. For **2**, the χ_M'' values were frequency (ν) dependent in the range of 0.1–1000 Hz in a zero magnetic field (Figures S10–S13), whereas for **1**, they were not. To clarify these differences, ac magnetic susceptibility measurements were performed in different magnetic fields at 1.8 K. When H was in the range of 0–5 kOe, the magnetization of both complexes underwent dual relaxation processes (Figure 5). As shown in Figure 6, the magnetic relaxation times (τ) calculated from the χ_M'' versus ν plot on the low ν side increased monotonically with an increase in H, and the τ values calculated from the high ν side reached a local maximum in specific applied H_{dc}. These results indicate that the maximum H_{dc} suppresses QTM and promotes a direct process [29], and the results can be reproduced using a mixture of QTM, direct and Raman processes with Equation (1) (Table S3):

$$\tau^{-1} = AH^nT + \frac{B_1}{1 + B_2H^2} + D. \tag{1}$$

In previous work, we have reported that compound **3** exhibited dual magnetic relaxation processes when H_{dc} was larger than 2.5 kOe [14]. To understand the details of the dual magnetic relaxation dynamics of **1** and **2**, we analyzed the ratio of relaxation time ρ (= τ_2/τ_1). The ρ values of 1 correspond to the occurrence of a single relaxation process in the Dy^{3+} SMM system. If the value is large enough (>1000), dual magnetic relaxation processes are observed separately [30]. Since the splitting of relaxation is observed at 0.25 kOe for **1** and **2**, it can be said that it responds more sensitively to H_{dc}. This is another indication that the ground states of Dy^{3+} ions are more complicated.

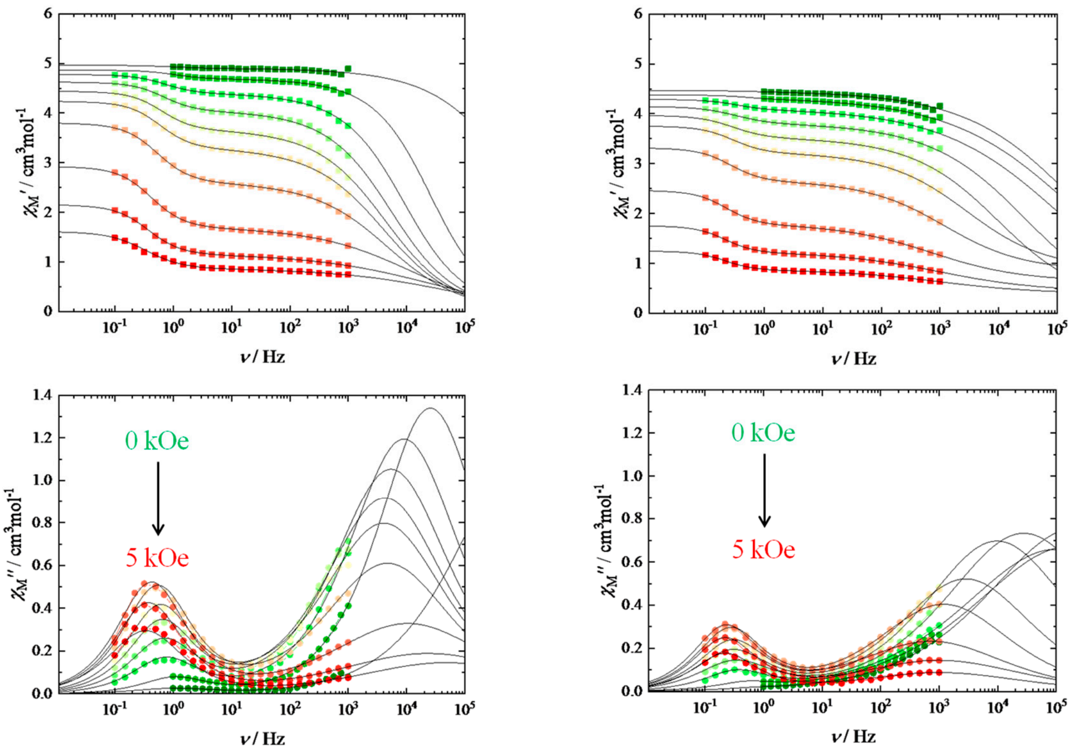

(**a**) (**b**)

Figure 5. ν dependence of the real (χ_M') and imaginary (χ_M'') parts of the ac susceptibilities of (**a**) **1** and (**b**) **2** in H_{dc} of 0–5 kOe at 1.8 K. Black solid lines were fitted by using an extended Debye model to obtain τ. Argand plots are in the supporting information (Figures S16 and S17)

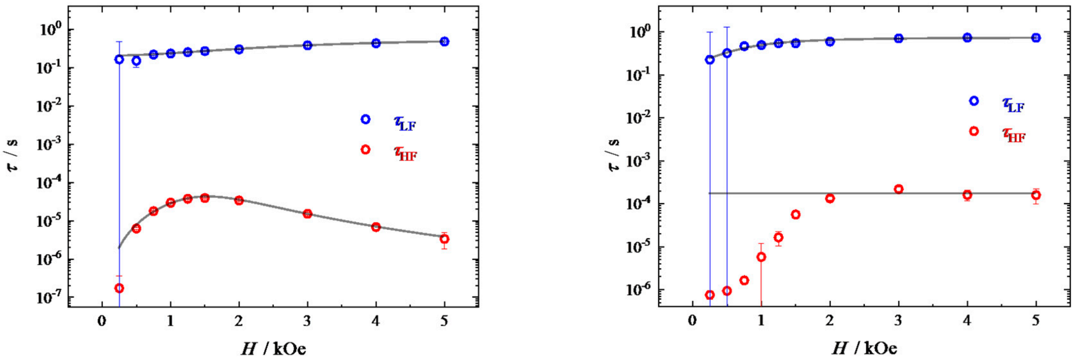

(**a**) (**b**)

Figure 6. (**a**) τ versus H for **1** at 1.8 K obtained from the least-squares fitting using an extended Debye model. τ from the high frequency region have the maxima each other. (**b**) τ versus H for **2**. The data were fitted using a mixture of as the quantum tunneling of the magnetization (QTM), direct and Raman processes with the parameters listed in the SI.

ν dependences of the χ_M'' values of **1** and **2** were measured in the range of 1–1000 Hz in various H_{dc}, and a split in the χ_M'' values was observed below 8 and 20 K, respectively. In a χ_M'' versus T plot, a peak top was observed in the T range below 2 K, indicating that the magnetic moment was not frozen or that a different relaxation processes, like QTM, was dominate. We used the Kramers–Kronig equation [31–35], which infers the pre-exponential factor τ_0 and the activation barrier U_{eff} from the $\chi_{\mathrm{M}}''/\chi_{\mathrm{M}}'$ versus T (2.5–4 K) plot, to fit the data:

$$\chi_{\mathrm{M}}''/\chi_{\mathrm{M}}' = \omega\tau, \tag{2}$$

$$\chi_{\mathrm{M}}''/\chi_{\mathrm{M}}' = \omega\tau_0 + \exp\left(U_{\mathrm{eff}}/T\right), \tag{3}$$

$$\ln\left(\chi_{\mathrm{M}}''/\chi_{\mathrm{M}}'\right) = \ln\left(\omega\tau_0\right) + U_{\mathrm{eff}}/T. \tag{4}$$

From a $\chi_{\mathrm{M}}''/\chi_{\mathrm{M}}'$ plot for **1**, U_{eff} was determined to be about 8.1 cm^{-1}, and $\tau_0 \approx 10^{-7}$ s. For **2**, U_{eff} was determined to be about 2.7 cm^{-1}, and $\tau_0 \approx 10^{-6}$ s (Figures S14 and S15). The small τ_0 indicates, that the contribution from an Orbach process becomes small. Figure 7 shows the relationship between U_{eff} and φ [15,16]. From this figure, as φ decreases from 45°, the activation energy tends to decrease. This is because a contribution from the off-diagonal LF terms promotes QTM, and during the conversion from SAP to SP geometries. Thus, B_2^0 becomes smaller, and off-diagonal terms B_4^4 and B_6^4 become larger, resulting in a narrower U_{eff}. It is thought that a small φ has a negative effect on the activation barrier. In other words, the small φ of **1** and **2** cause a decrease in the activation barrier.

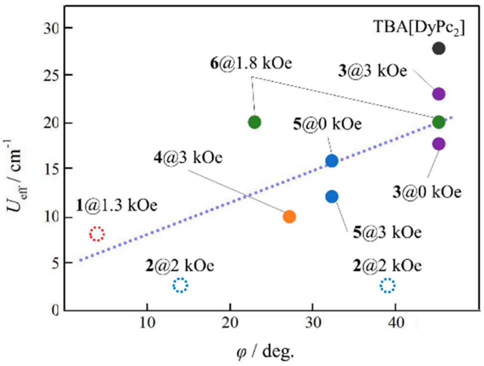

Figure 7. U_{eff} versus φ plots for related Dy^{3+}-Pc single molecule magnets (SMMs). Blue dotted lines are guides only. Dotted circles indicate the values for **1** and **2**, and the color dots indicate **3**–**6** in H_{dc}. Since **2** and **6** have two different Dy^{3+} sites, the distribution of which could not be separated distribution, both φ values are displayed.

To investigate the magnetic relaxation properties of **1** and **2** at low T, ν dependence measurements were performed in an applied H_{dc} in the T range of 1.8–4.5 K. An Argand plot for both complexes showed that a dual magnetic relaxation process occurred. τ for each component was calculated by fitting the imaginary component of the ac magnetic susceptibility with the extended Debye model (Equations S2 and S3, Figure 8), and using those values, an Arrhenius plot was obtained (Figure 9). From a fitting with Equation (5) on the values for **1**, τ obtained from the low ν side indicates that a QTM process independent of T occurs, and that obtained from the high ν side is proportional to T^{-9}, meaning that it is a Raman process (Table S4). However, the fitting of the data for **1** is not accurate due to large deviation in the τ values. In particular, when τ values at $T > 2.5$ K, the spin dynamics of **1** could not be determined. On the other hand, for **2**, τ obtained from the low ν side is proportional to $T^{-1.7}$, and that obtained from the high ν side indicates that a direct process occurs. For both complexes, the lowest ground state estimated from the crystal structure is expected to contain a large amount of mixing. Therefore, even when a complex has crystallographically equivalent Dy^{3+} ions, dual relaxation processes occur between mixed states in an applied magnetic field. In the case of **1**, the $D_{4\mathrm{h}}$ symmetry around the Dy^{3+} ion has a large effect on the off-diagonal term, causing QTM to be dominant. In addition, T is proportional to $\mathrm{n} \approx -2$ which could be reproduced using a PB process to fit the data.

However, since Raman processes can involve acoustic-optical phonons (n = 1–6) [18], it is difficult to separate each contribution due to the complicated ground state of **2**.

$$\tau^{-1} = AH^{n}T + CT^{m} + \tau_{\mathrm{QTM}}^{-1}. \quad (5)$$

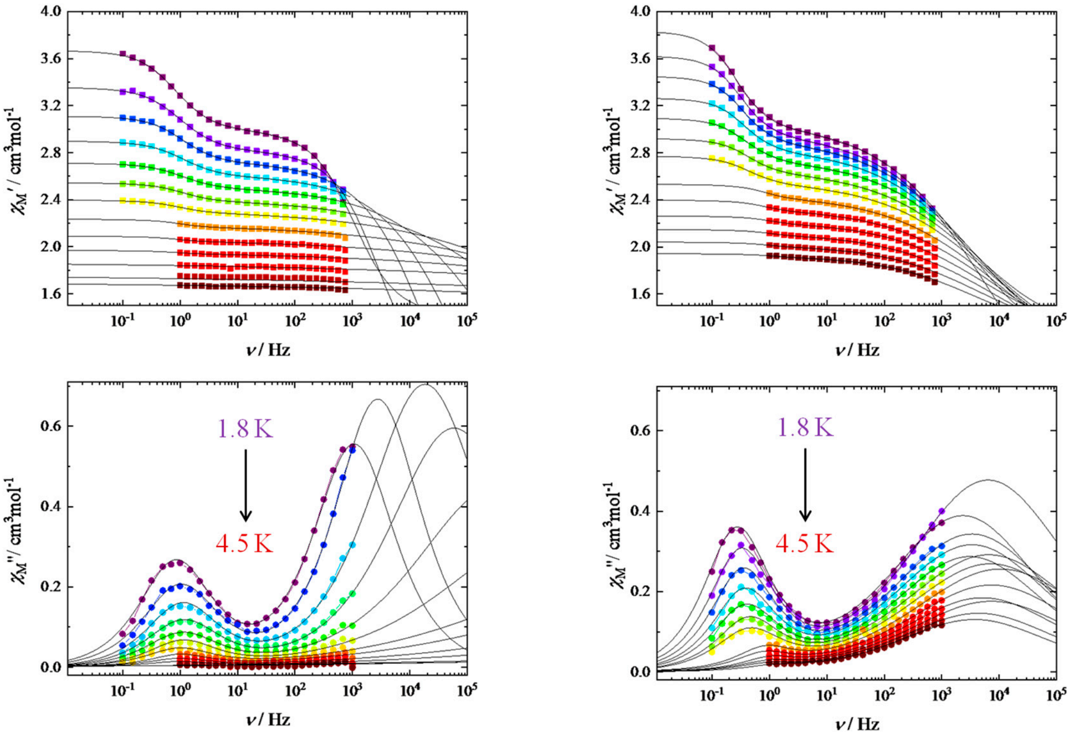

(**a**) (**b**)

Figure 8. ν dependence of the out of phase (χ_{M}'') parts of the ac magnetic susceptibilities of **1** (**a**) and **2** (**b**) measured in the T range of 1.8–4.5 K in H_{dc}. Black solid lines were fitted by using an extended Debye model to obtain τ. Argand plots are located in the supporting information (Figures S18 and S19).

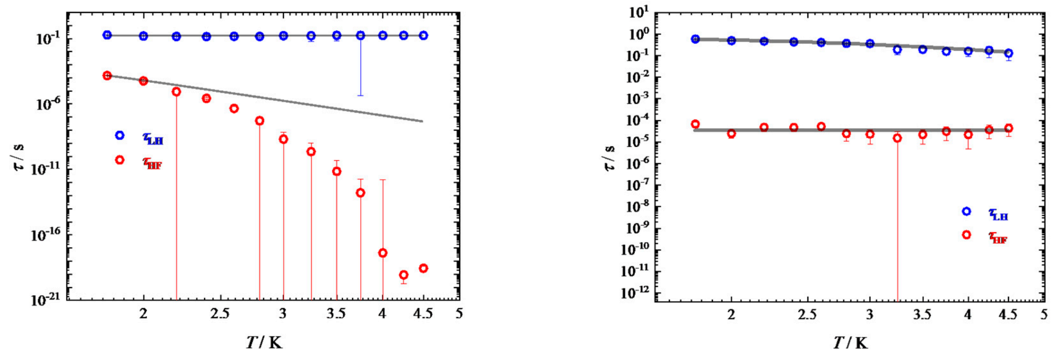

(**a**) (**b**)

Figure 9. An Arrhenius plot for (**a**) **1** and (**b**) **2**, for which the τ values were obtained from χ_{M}'' versus ν plots in H_{dc} of 1.3 and 2 kOe, respectively, in the T range of 1.8–4.5 K. The blue circles indicate the τ values from the low ν region and red circles indicate those from the high ν region. Black solid lines were fitted by using Equation (5).

3. Materials and Methods

3.1. Synthesis

Solvents were used without further purification. Dy(acac)$_3$·4H$_2$O and the free ligand were purchased from TCI Tokyo Chemical Industry Co., LTD, Tokyo, Japan. Dy(acac)$_3$·4H$_2$O (180 mg, 0.40 mmol) and H$_2$TTP (tetraphenylporphyrin) (150 mg, 0.25 mmol) were added to dry 1,2,4-trichlorobenzene (40 mL). The solution was refluxed under nitrogen for 4 h. After cooling, Li$_2$Pc (158 mg, 0.60 mmol) was added to the mixture. Then, the solution was refluxed for 12 h. After cooling, the reaction mixture was added to n-hexane (500 mL). The obtained solid was purified by using column chromatography on silica gel with chloroform as the eluent. [(TTP)Dy(Pc)Dy(TTP)] (**1**) was obtained from a deep brownish red fraction, which was the first fraction, by removing the solvent (16%), and [(Pc)Dy(Pc)Dy(TTP)] (**2**) was obtained from the dark green second fraction (34%). Spectroscopic data used for characterization are described in the SI (Figures S5 and S6). Column chromatography (C-200 silica gel, Wako and Sephadex G-10, Pharmacia Biotech) was used to remove the remaining impurities. Dark red block crystals of **1** were obtained from chloroform/n-hexane (27 mg). ESI-MS: m/z (%): 2062.47242 (100) [M−1$^+$] (Figures S1 and S2); elemental analysis calcd (%) for $C_{120}H_{72}N_{16}Dy_2 \cdot 4CHCl_3$: C 58.62, H 3.02, N 8.82; found: C 60.03, H 3.21, N 8.89. Black fine needle crystals of **2** were obtained from chloroform/n-hexane (83 mg). ESI-MS: m/z (%): 1962.38956 (100) [M$^+$] (Figure S3 and S4); elemental analysis calcd (%) for $C_{108}H_{60}N_{20}Dy_2 \cdot CHCl_3$: C 60.01, H 2.84, N 12.72; found: C 62.91, H 3.28, N 13.36. The results of the elemental analysis for **2** indicates desorption of some of the $CHCl_3$ molecules compared with the number of $CHCl_3$ molecules calculated from the crystal structure.

3.2. Physical Measurements

Elemental analyses were conducted on a PerkinElmer 240C elemental analyzer (PerkinElmer, Waltham, MA, USA) at the Research and Analytical Centre for Giant Molecules, Tohoku University. UV-Vis-NIR spectra were acquired using $CHCl_3$ solution on a Shimadzu UV-3100pc (Shimadzu, Kyoto, Japan). IR spectroscopy was performed on ATR method on FT/IR-4200 spectrometer at 298 K. Magnetic susceptibility measurements were conducted on a Quantum Design SQUID magnetometer MPMS-XL and MPMS-3 (Quantum Design, San Diego, CA, USA) in the T and dc field ranges of 1.8–300 K and ±50 kOe, respectively. AC measurements were performed in the frequency range of 0.1–1000 Hz with an ac field amplitude of 3 Oe. A polycrystalline sample suspended in n-eicosane was used for the measurements. Crystallographic data for **1** and **2** were collected at 120 K on a Rigaku Saturn724+ CCD Diffractometer (Rigaku, Tokyo, Japan) with graphite-monochromated Mo Kα radiation (λ = 0.71075 Å) produced using a VariMax microfocus X-ray rotating anode source. Single crystals with dimensions of $0.10 \times 0.07 \times 0.01$ mm^3 (**1**) and $0.15 \times 0.20 \times 0.04$ mm^3 (**2**) were used. Data processing was conducted using the Crystal Clear crystallographic software package [36]. The structures were solved by using direct methods using SIR-92 [37]. Refinement was carried out using the Yadokari-XG package [38] and SHELXT. The non-Hydrogen atoms were refined anisotropically using weighted full-matrix least squares on F. Hydrogen atoms attached to the carbon atoms were fixed using idealized geometries and refined using a riding model. CCDC 1940003 for **1** and 1940004 for **2**. Powder X-ray diffraction was conducted on a Bruker AXS D2 phaser (Bruker Corporation Billerica, MA, USA).

4. Conclusions

Complexes **1** and **2** were synthesized similar to previously reported Dy^{3+}-Pc complexes with a TPP^{2-} ligand. The TPP^{2-} ligands induce a smaller twist angle (φ) between the ligands than those in the previous complexes due to the effects of steric repulsion from the phenyl group. Although **1** has D_{4h} symmetry due to the two TPP^{2-} ligands, **2** has lower symmetry due to having only one TPP^{2-}. From dc magnetic measurements on both complexes, the $\chi_M T$ values decreased due to depopulation. Measurement of M-HT^{-1} indicated uniaxial anisotropy, but it is smaller than the expected values for a pseudospin model. No hysteresis opening at 1.8 K was observed, suggesting a mixture of ground states, which is consistent with the estimation of the ground state using the value of α obtained from the crystal structure data. In addition, dual slow magnetization relaxation was observed for both complexes from ac magnetic susceptibility measurements in an applied H_{dc}. U_{eff} calculated by using the Kramers–Kronig equation is very small and corresponded to the tendency of previous triple-decker compounds to decrease with decrease of φ. From above the results, **1** and **2** are field-induced SMMs. For **1**, QTM and Raman processes occur due to the symmetry of $D_{4\mathrm{h}}$, whereas for **2**, mixed relaxation (Raman, PB) and QTM processes occur. The contributions of the Raman and PB processes must be clarified. The magnetic processes involve spin relaxation in mixed ground states, and the off-diagonal term is dominant. This is different from conventional dinuclear Dy^{3+} complexes. Multiple relaxation processes could be turned on by adjusting φ to 4° (**1**) and 14° (**2**), and this can be used to prepare functional SMMs whose characteristics can be switched on and off by changing φ.

Supplementary Materials: The following are available online at http://www.mdpi.com/2312-7481/5/4/65/s1. Figure S1: ESI-MS spectrum of **1** in $\mathrm{CHCl_3}$. The peak at 2062.47242 corresponds to [M-1$^+$]. Figure S2: Experimental (top) and simulated (bottom) ESI-MS spectra of **1** in $\mathrm{CHCl_3}$. The peak at 2062.47242 corresponds to [M−1$^+$]. Figure S3: ESI-MS spectrum of **2** in $\mathrm{CHCl_3}$. The peak at 1962.38956 corresponds to [M$^+$]. Figure S4: Experimental (top) and simulated (bottom) ESI-MS spectra of **2** in $\mathrm{CHCl_3}$. The peak at 1962.38956 corresponds to [M$^+$]. Figure S5: IR spectrum for **1** (top) and **2** (bottom) by using an ATR method at 298 K. Figure S6: UV-vis-NIR spectra for **1** (top) and **2** (bottom) in $\mathrm{CHCl_3}$ (5.1×10^{-3} (**1**), and 4.7×10^{-3} (**2**)) at 298 K. Figure S7: PXRD patterns for 1 (top) and 2 (bottom). Figure S8: Curie–Weiss plot for **1**. Linear approximation is performed over the entire T range, from which the values of Curie constant (C) (28.50 cm^3 K mol^{-1}) and Weiss constant (θ) (–2.33 K) were obtained. Figure S9: Curie–Weiss plot for **2**. Linear approximation is performed over the entire T range, from which the values of Curie constant (C) (28.20 cm^3 K mol^{-1}) and Weiss constant (θ) (–1.97 K) were obtained. Figure S10: Frequency (ν) and temperature (T) dependences of the (**a**) in-phase (χ_{M}') and (**b**) out-of-phase (χ_{M}'') ac magnetic susceptibilities of **1** in 0 kOe. Figure S11: Frequency (ν) and temperature (T) dependences of the (**a**) in-phase (χ_{M}') and (**b**) out-of-phase (χ_{M}'') ac magnetic susceptibilities of **2** in 0 kOe. Figure S12: Frequency (ν) and temperature (T) dependences of the (**a**) in-phase (χ_{M}') and (**b**) out-of-phase (χ_{M}'') ac magnetic susceptibilities of **1** in 1.3 kOe. Figure S13: Frequency (ν) and temperature (T) dependences of the (**a**) in-phase (χ_{M}') and (**b**) out-of-phase (χ_{M}'') ac magnetic susceptibilities of **2** in 2 kOe. Figure S14: $\chi_{\mathrm{M}}''/\chi_{\mathrm{M}}'$ versus T (2.5–4 K) plot for **1**. Figure S15: $\chi_{\mathrm{M}}''/\chi_{\mathrm{M}}'$ versus T (2.5–4 K) plot for **2**. Figure S16: Argand plots (χ_{M}'' versus χ_{M}') for **1** at 1.8 K in several dc magnetic fields (0-5 kOe). Black solid lines were guides for eye. Figure S17: Argand plots (χ_{M}'' versus χ_{M}') for **2** at 1.8 K in several dc magnetic fields in the range of 0–5 kOe. Black solid lines were guides for eye. Figure S18: Argand plots (χ_{M}'' versus χ_{M}') for **1** in 1.3 kOe in the T range of 1.8–4.5 K. Black solid lines are guides for the eye. Figure S19: Argand plots (χ_{M}'' versus χ_{M}') for **1** in 2 kOe field in the T range of 1.8–4.5 K. Black solid lines are guides for the eye. Table S1: Selected crystallographic data for **1** and **2**. Table S2: Selected crystallographic data for **1** and **2**. Table S3: Parameters for fitting the τ verses H plots. Table S4: Parameters of fitting for τ verses T plot.

Author Contributions: Conceptualization, K.K.; Data curation, K.K.; Formal analysis, T.S. and S.M.; Funding acquisition, K.K. and M.Y.; Investigation, T.S. and S.M.; Methodology, K.K.; Project administration, K.K. and M.Y.; Supervision, K.K.; Validation, K.K.; Visualization, B.K.B.; Writing—original draft, T.S.; Writing—review & editing, K.K., B.K.B and M.Y.

Funding: This work was supported by a Grant-in-Aid for Scientific Research (S) (grant no. 20225003), Grant-in-Aid for Young Scientists (B) (grant no. 24750119), Grant-in-Aid for Scientific Research (C) (grant no. 15K05467) from the Ministry of Education, Culture, Sports, Science, Technology, Japan (MEXT), CREST (JPMJCR12L3) from JST, a Grant-in-aid for JSPS fellows from the Japan Society for the Promotion of Science (JSPS) (25·2441), and Tohoku University Division for International Advanced Research and Education (DIARE). M.Y. is grateful for the support from the 111 project (B18030) from China. S.M. acknowledges the support by MD-program of Tohoku Univ.

Conflicts of Interest: The authors declare no conflict of interest.

References

1. Sessoli, R.; Gatteschi, D.; Caneschi, A. Magnetic bistability in a metal-ion cluster. *Nature* **1993**, *363*, 141–143. [CrossRef]
2. Wernsdorfer, W.; Sessoli, R. Quantum Phase Interference and Parity Effects in Magnetic Molecular Clusters. *Science* **1999**, *284*, 133–136. [CrossRef] [PubMed]
3. Choi, K.Y.; Wang, Z.; Nojiri, H.; Van Tol, J.; Kumar, P.; Lemmens, P.; Bassil, B.S.; Kortz, U.; Dalal, N.S. Coherent manipulation of electron spins in the (Cu3) spin triangle complex impregnated in nanoporous silicon. *Phys. Rev. Lett.* **2012**, *108*, 1–5. [CrossRef] [PubMed]

4. Vincent, R.; Klyatskaya, S.; Ruben, M.; Wernsdorfer, W.; Balestro, F. Electronic read-out of a single nuclear spin using a molecular spin transistor. *Nature* **2012**, *488*, 357–360. [CrossRef]
5. Collauto, A.; Mannini, M.; Sorace, L.; Barbon, A.; Brustolon, M.; Gatteschi, D. A slow relaxing species for molecular spin devices: EPR characterization of static and dynamic magnetic properties of a nitronyl nitroxide radical. *J. Mater. Chem.* **2012**, *22*, 22272–22281. [CrossRef]
6. Wedge, C.J.; Timco, G.A.; Spielberg, E.T.; George, R.E.; Tuna, F.; Rigby, S.; McInnes, E.J.L.; Winpenny, R.E.P.; Blundell, S.J.; Ardavan, A. Chemical engineering of molecular qubits. *Phys. Rev. Lett.* **2012**, *108*, 1–5. [CrossRef]
7. Aguilà, D.; Barrios, L.A.; Velasco, V.; Roubeau, O.; Repollés, A.; Alonso, P.J.; Sesé, J.; Teat, S.J.; Luis, F.; Aromí, G. Heterodimetallic [LnLn′] lanthanide complexes: Toward a chemical design of two-qubit molecular spin quantum gates. *J. Am. Chem. Soc.* **2014**, *136*, 14215–14222. [CrossRef]
8. Long, J.; Selikhov, A.N.; Mamontova, E.; Lyssenko, K.A.; Guari, Y.; Larionova, J.; Trifonov, A.A. Single-molecule magnet behaviour in a Dy(iii) pentagonal bipyramidal complex with a quasi-linear Cl-Dy-Cl sequence. *Dalt. Trans.* **2019**, *48*, 35–39. [CrossRef]
9. Guo, F.S.; Day, B.M.; Chen, Y.C.; Tong, M.L.; Mansikkamäki, A.; Layfield, R.A. A Dysprosium Metallocene Single-Molecule Magnet Functioning at the Axial Limit. *Angew. Chem. Int. Ed.* **2017**, *56*, 11445–11449. [CrossRef]
10. Day, B.M.; Guo, F.S.; Layfield, R.A. Cyclopentadienyl Ligands in Lanthanide Single-Molecule Magnets: One Ring to Rule Them All? *Acc. Chem. Res.* **2018**, *51*, 1880–1889. [CrossRef]
11. Tanaka, D.; Inose, T.; Tanaka, H.; Lee, S.; Ishikawa, N.; Ogawa, T. Proton-induced switching of the single molecule magnetic properties of a porphyrin based $\mathrm{Tb^{III}}$ double-decker complex. *Chem. Commun.* **2012**, *48*, 7796–7798. [CrossRef] [PubMed]
12. Horii, Y.; Horie, Y.; Katoh, K.; Breedlove, B.K.; Yamashita, M. Changing Single-Molecule Magnet Properties of a Windmill-Like Distorted Terbium(III) α-Butoxy-Substituted Phthalocyaninato Double-Decker Complex by Protonation/Deprotonation. *Inorg. Chem.* **2018**, *57*, 565–574. [CrossRef] [PubMed]
13. Horii, Y.; Katoh, K.; Yasuda, N.; Breedlove, B.K.; Yamashita, M. Effects of f-f interactions on the single-molecule magnet properties of terbium(iii)-phthalocyaninato quintuple-decker complexes. *Inorg. Chem.* **2015**, *54*, 3297–3305. [CrossRef] [PubMed]
14. Katoh, K.; Aizawa, Y.; Morita, T.; Breedlove, B.K.; Yamashita, M. Elucidation of Dual Magnetic Relaxation Processes in Dinuclear Dysprosium(III) Phthalocyaninato Triple-Decker Single-Molecule Magnets Depending on the Octacoordination Geometry. *Chem. A Eur. J.* **2017**, *23*, 15377–15386. [CrossRef] [PubMed]
15. Ishikawa, N.; Sugita, M.; Okubo, T.; Tanaka, N.; Iino, T.; Kaizu, Y. Determination of ligand-field parameters and f-electronic structures of double-decker bis(phthalocyaninato)lanthanide complexes. *Inorg. Chem.* **2003**, *42*, 2440–2446. [CrossRef] [PubMed]
16. Ishikawa, N.; Iino, T.; Kaizu, Y. Interaction between f-electronic systems in dinuclear lanthanide complexes with phthalocyanines. *J. Am. Chem. Soc.* **2002**, *124*, 11440–11447. [CrossRef]
17. Tran-Thi, T.H.; Mattioli, T.A.; Chabach, D.; Cian, A.D.; Weiss, R. Hole localization or delocalization? An optical, raman, and redox study of lanthanide porphyrin-phthalocyanine sandwich-type heterocomplexes. *J. Phys. Chem.* **1994**, *98*, 8279–8288. [CrossRef]
18. Zhang, P.; Guo, Y.N.; Tang, J. Recent advances in dysprosium-based single molecule magnets: Structural overview and synthetic strategies. *Coord. Chem. Rev.* **2013**, *257*, 1728–1763. [CrossRef]
19. Sorace, L.; Benelli, C.; Gatteschi, D. Lanthanides in molecular magnetism: Old tools in a new field. *Chem. Soc. Rev.* **2011**, *40*, 3092–3104. [CrossRef]
20. Katoh, K.; Morita, T.; Yasuda, N.; Wernsdorfer, W.; Kitagawa, Y.; Breedlove, B.K.; Yamashita, M. Tetranuclear Dysprosium(III) Quintuple-Decker Single-Molecule Magnet Prepared Using a π-Extended Phthalocyaninato Ligand with Two Coordination Sites. *Chem. A Eur. J.* **2018**, *24*, 15522–15528. [CrossRef]
21. Katoh, K.; Horii, Y.; Yasuda, N.; Wernsdorfer, W.; Toriumi, K.; Breedlove, B.K.; Yamashita, M. Multiple-decker phthalocyaninato dinuclear lanthanoid(iii) single-molecule magnets with dual-magnetic relaxation processes. *Dalt. Trans.* **2012**, *41*, 13582–13600. [CrossRef] [PubMed]
22. Liu, J.L.; Chen, Y.C.; Tong, M.L. Symmetry strategies for high performance lanthanide-based single-molecule magnets. *Chem. Soc. Rev.* **2018**, *47*, 2431–2453. [CrossRef] [PubMed]

23. Bi, Y.; Guo, Y.N.; Zhao, L.; Guo, Y.; Lin, S.Y.; Jiang, S.D.; Tang, J.; Wang, B.W.; Gao, S. Capping ligand perturbed slow magnetic relaxation in dysprosium single-ion magnets. *Chem. A Eur. J.* **2011**, *17*, 12476–12481. [CrossRef] [PubMed]
24. Damjanovic, M.; Katoh, K.; Yamashita, M.; Enders, M. Combined NMR analysis of huge residual dipolar couplings and pseudocontact shifts in terbium(III)-phthalocyaninato single molecule magnets. *J. Am. Chem. Soc.* **2013**, *135*, 14349–14358. [CrossRef] [PubMed]
25. Zou, L.; Zhao, L.; Chen, P.; Guo, Y.N.; Guo, Y.; Li, Y.H.; Tang, J. Phenoxido and alkoxido-bridged dinuclear dysprosium complexes showing single-molecule magnet behaviour. *Dalt. Trans.* **2012**, *41*, 2966–2971. [CrossRef]
26. Katoh, K.; Breedlove, B.K.; Yamashita, M. Symmetry of octa-coordination environment has a substantial influence on dinuclear TbIII triple-decker single-molecule magnets. *Chem. Sci.* **2016**, *7*, 4329–4340. [CrossRef]
27. Chilton, N.F.; Anderson, R.P.; Turner, L.D.; Soncini, A.; Murray, K.S. PHI: A powerful new program for the analysis of anisotropic monomeric and exchange-coupled polynuclear d- and f-block complexes. *J. Comput. Chem.* **2013**, *34*, 1164–1175. [CrossRef]
28. Moreno Pineda, E.; Chilton, N.F.; Marx, R.; Dörfel, M.; Sells, D.O.; Neugebauer, P.; Jiang, S.D.; Collison, D.; Van Slageren, J.; McInnes, E.J.L.; et al. Direct measurement of dysprosium(III)$\cdots$dysprosium(III) interactions in a single-molecule magnet. *Nat. Commun.* **2014**, *5*, 1–7. [CrossRef]
29. Ding, Y.S.; Yu, K.X.; Reta, D.; Ortu, F.; Winpenny, R.E.P.; Zheng, Y.Z.; Chilton, N.F. Field- and temperature-dependent quantum tunnelling of the magnetisation in a large barrier single-molecule magnet. *Nat. Commun.* **2018**, *9*, 1–10. [CrossRef]
30. Guo, Y.N.; Xu, G.F.; Guo, Y.; Tang, J. Relaxation dynamics of dysprosium(iii) single molecule magnets. *Dalt. Trans.* **2011**, *40*, 9953–9963. [CrossRef]
31. Gass, I.A.; Moubaraki, B.; Langley, S.K.; Batten, S.R.; Murray, K.S. A π-π 3D network of tetranuclear μ2/μ3- carbonato Dy(iii) bis-pyrazolylpyridine clusters showing single molecule magnetism features. *Chem. Commun.* **2012**, *48*, 2089–2091. [CrossRef] [PubMed]
32. Ferrando-Soria, J.; Cangussu, D.; Eslava, M.; Journaux, Y.; Lescouëzec, R.; Julve, M.; Lloret, F.; Pasán, J.; Ruiz-Pérez, C.; Lhotel, E.; et al. Rational enantioselective design of chiral heterobimetallic single-chain magnets: Synthesis, crystal structures and magnetic properties of oxamato-bridged MIICuII chains (M = Mn, Co). *Chem. A Eur. J.* **2011**, *17*, 12482–12494. [CrossRef] [PubMed]
33. Bartolomé, J.; Filoti, G.; Kuncser, V.; Schinteie, G.; Mereacre, V.; Anson, C.E.; Powell, A.K.; Prodius, D.; Turta, C. Magnetostructural correlations in the tetranuclear series of {Fe3 LnO2} butterfly core clusters: Magnetic and Mössbauer spectroscopic study. *Phys. Rev. B Condens. Matter Mater. Phys.* **2009**, *80*, 1–16. [CrossRef]
34. Luis, F.; Bartolomé, J.; Fernández, J.; Tejada, J.; Hernández, J.; Zhang, X. Thermally activated and field-tuned tunneling inAc studied by ac magnetic susceptibility. *Phys. Rev. B Condens. Matter Mater. Phys.* **1997**, *55*, 11448–11456. [CrossRef]
35. Nakanishi, R.; Yatoo, M.A.; Katoh, K.; Breedlove, B.K.; Yamashita, M. Dysprosium Acetylacetonato Single-molecule magnet encapsulated in Carbon Nanotubes. *Materials (Basel)* **2017**, *10*, 7. [CrossRef] [PubMed]
36. Rigaku Corporation. *Crystal Clear-SM, 1.4.0 SP1*; Rigaku Corporation: Tokyo, Japan, 17 April 2008.
37. Altomare, A.; Burla, M.C.; Camalli, M.; Cascarano, G.L.; Giacovazzo, C.; Guagliardi, A.; Moliterni, A.G.G.; Polidori, G.; Spagna, R. SIR97: A new tool for crystal structure determination and refinement. *J. Appl. Crystallogr.* **1999**, *32*, 115–119. [CrossRef]
38. Kabuto, C.; Akine, S.; Nemoto, T.; Kwon, E.J.; Wakita, K. Yadokari-XG, Software for Crystal Structure Analyses, 2001; Release of Software (Yadokari-XG 2009) for Crystal Structure Analyses. *Cryst. Soc. Jpn.* **2010**, *51*, 218–224. [CrossRef]